JOURNAL OF GEOPHYSICAL RESEARCH, VOL. 106, NO. C4, PAGES 6943–6955, APRIL 15, 2001

Role of ocean dynamics in determining the mean seasonal cycle of the South China Sea surface temperature

Tangdong Qu

International Pacific Research Center, School of Ocean and Earth Science and Technology, University of Hawaii at Manoa, Honolulu, Hawaii

Abstract. The mean seasonal cycle of surface heat budget is examined using historical temperature data combined with climatological wind stress and surface heat flux in the South China Sea. In most parts of the basin, we see a negative correlation between sea surface temperature (SST) and mixed layer depth (MLD); that is, SST tends to be higher (lower) when MLD is shallower (deeper). Given the characteristics of the MLD distribution, we further partition the South China Sea into four smaller areas: one along the continental slope south of China, one off west Luzon, one in the central part of the basin, and one near the coast of Vietnam. Heat budget assessment in these smaller areas indicates that although surface heat flux is fundamental to the mean seasonal cycle of SST, the effect of ocean dynamics is not negligible. Adding the contribution of ocean dynamics better explains the SST tendency. Ekman advection forced by the northeast monsoon is the primary heating process in winter but becomes less important as the horizontal temperature gradient decreases in the following seasons. Vertical entrainment is effective at cooling when the southwest monsoon prevails, which works against the surface heating and leads to a decrease of SST by up to 5 months earlier than surface heat flux starts to cool the ocean.

1. Introduction

The South China Sea is the largest marginal sea in the southeast Asian waters, connecting in the south with the Java and Sulu Seas through a number of shallow passages and in the north with the Pacific through the deep Luzon strait (Figure 1a). Because of its geographical location, the sea surface temperature (SST) in the South China Sea has remarkable characteristics associated with the Asian monsoon and rainfall [*Shen and Lau*, 1995; *Tomita and Yasunari*, 1996]. On seasonal timescales both cool and warm anomalies of SST from its annual mean value have been reported. These include a cool anomaly east of Vietnam in summer, a cool anomaly northwest of Luzon in winter, and a warm anomaly in the central South China Sea in spring [e.g., *Chu et al*., 1997, 1998]. These anomalies of SST are believed to be important to the seasonal transition of monsoon [*Chu and Chang*, 1997]. Recent studies [e.g., *He et al*., 1997; *Ose et al*., 1997] also suggest that the South China Sea SST variability has a close relationship with El Niño–Southern Oscillation (ENSO) and the North Pacific decadal signal as well.

The mechanisms that cause the South China Sea SST variability are not well understood. Several earlier studies [e.g., *Tomita and Yasunari*, 1996; *Ose et al*., 1997] have successfully related it to the large-scale circulation in the atmosphere, but very little is known about the effect of ocean dynamics. In this study we utilize all existing temperature profiles (mainly expendable bathythermograph (XBT) measurements), along with the climatologies of wind stress and surface heat flux, to assess the mean seasonal cycle of surface heat budget. Although assessment of surface heat budget based on climatological data may not be especially accurate, it provides at least a background for understanding how SST is maintained and changed. We expect that a successful identification of the role of ocean dynamics in determining the mean seasonal cycle of SST will give useful hints for further investigation of lower-frequency variabilities in the South China Sea.

Paper number 2000JC000479.
0148-0227/01/2000JC000479$09.00

The remaining part of the paper is arranged as follows. In section 2 we describe the data and methods of analysis. In section 3 we provide a general description of the South China Sea. In section 4 we focus on the relationship between SST and mixed layer depth (MLD). In section 5 we assess the surface heat budget. In section 6 we discuss dynamics related to the onset of the southwest monsoon. In section 7 we summarize all the results.

2. Data and Methods of Analysis

Historical temperature profiles recorded on the CD-ROMs of the "World Ocean Atlas 1994" of National Oceanic and Atmospheric Administration (NOAA)/National Environmental Satellite Data and Information Service (NESDIS)/National Oceanographic Data Center (NODC) in the region 3°–25°N, 105°–120°E are used for this study (Figure 1b). The primary editing procedure includes removal of profiles with obviously erroneous records and profiles with large spikes (e.g., temperature greater than 35°C and lower than 0°C). After these editing processes the data set consists of 74,139 temperature profiles over the entire basin of the South China Sea. The temporal and spatial distributions of the data are irregular. In time they spanned the period from the 1920s to the beginning of 1990s, with a heavily sampled period in 1965–1975; no obvious bias in the density of sampling was apparent toward any month of the year. In space the upper ocean was best sampled in the northern and central South China Sea, basically north of the line from 109°E, 7°N to 120°E, 13°N, and there were 2138

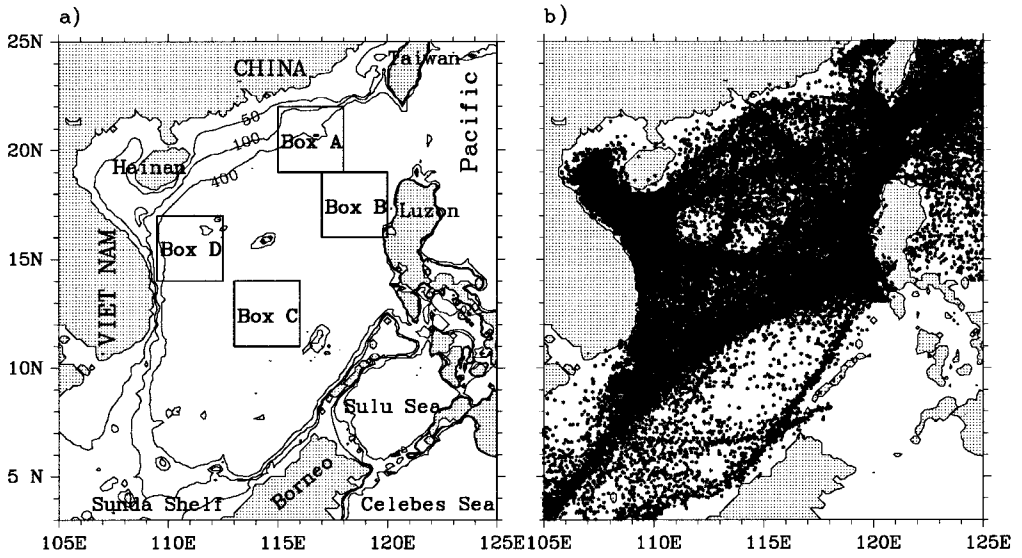

Figure 1. (a) Bottom topography and (b) station distribution in the South China Sea. Four smaller areas selected for heat budget analysis, namely, boxes A, B, C, and D are shown.

profiles in box A, 3682 profiles in box B, 2651 profiles in box C, and 5794 profiles in box D (Figure 1a).

Monthly mean temperatures are obtained by averaging on a series uniform pressure surfaces with a 10 dbar vertical resolution in a 0.5° × 0.5° horizontal grid, regardless of the year of observations. Standard deviations are also calculated during the averaging process. Near the sea surface, monthly temperature standard deviation is of the order 0.15°C based on typical ensembles of 7–10 observations at each grid. These values are then used to edit the resulting mean at each grid. Observations that differed from the grid mean by more than 3 standard deviations are discarded. The mean temperature fields are finally smoothed using Gaussian filter with an *e*-folding scale of 150 km.

The present temperature data better resolve the upper layer thermal structure than *Levitus*' [1982] climatology, including the West Luzon eddy, East Vietnam eddy, and many detailed aspects associated with the narrow western boundary currents [see *Qu*, 2000]. As one would expect, most of these phenomena are not markedly evident in Levitus' climatology as a result of smoothing over 700 km.

3. General Characteristics

3.1. Sea Surface Temperature

The distribution of the South China Sea SST has been described by several earlier studies [e.g., *Chu et al*., 1997]. In the interest of brevity, only a brief summary is presented here. In the mean, surface isotherms are oriented chiefly northeast-southwest, with SST decreasing from about 28.5°C off Borneo to <26.0°C near the southern coast of China (Figure 2a). Its seasonal variability (Figure 2b), measured by the peak-to-peak amplitude, is larger (>6.0°C) in the north and smaller

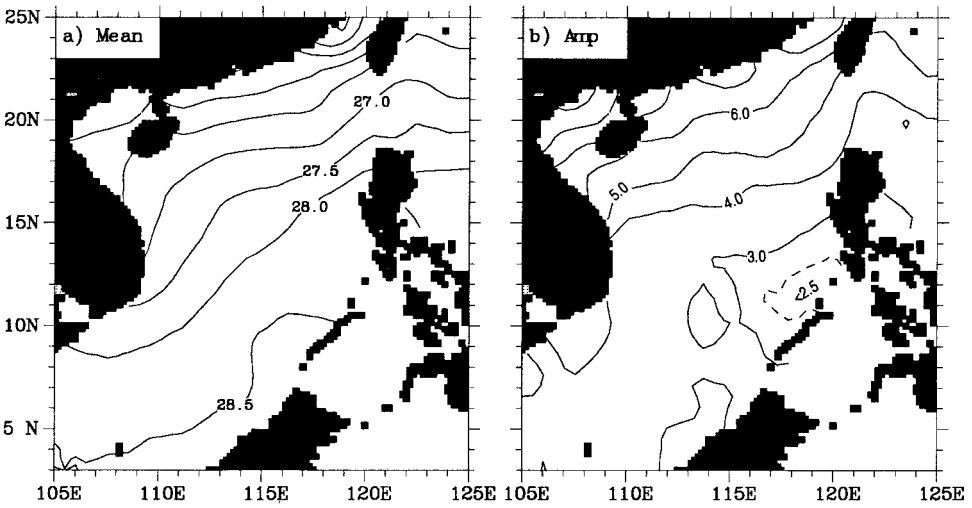

Figure 2. (a) Annual mean and (b) peak-to-peak amplitude of the seasonal variation of sea surface temperature (°C).

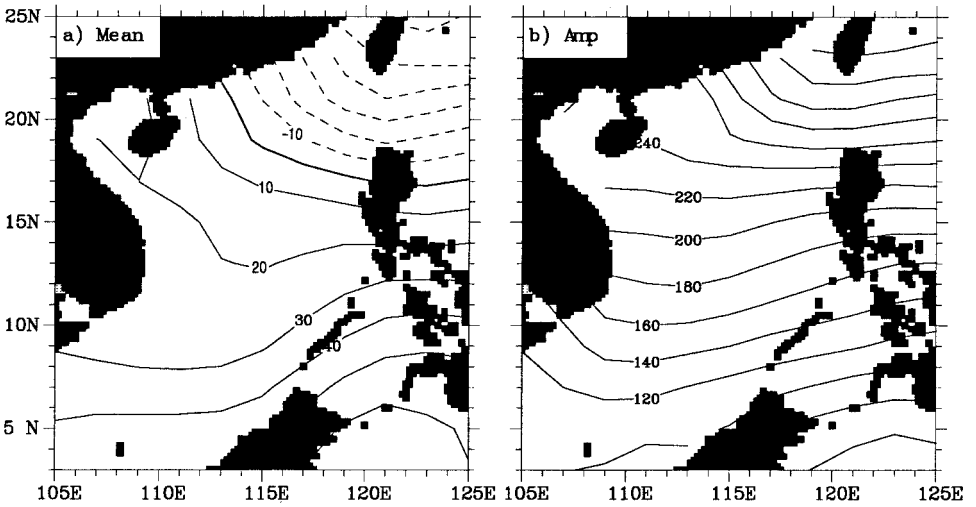

Figure 3. Same as Figure 2 except for surface heat flux (W m^{-2}) in *Oberhuber*'s [1988] climatology.

(<4.0°C) in the south, with a minimum (<2.5°C) in the southeast corner of the basin.

3.2. Surface Heat Flux

Net surface heat flux is difficult to estimate. Most of the atlases available presently were derived using empirical parameterizations of the air-sea fluxes based on marine observations. Figure 3 shows the results from *Oberhuber*'s [1988] climatology in a 2° × 2° horizontal grid. In the mean the atmosphere heats the ocean in the south (maximum heating rate ~40 W m^{-2}) and cools it in the north (ocean cooling exceeding −40 W m^{-2}), with the zero line extending roughly from 113°E, 21°N to 120°E, 17°N (Figure 3a). The seasonal variation of the surface heat flux is extremely large; its peak-to-peak amplitude ranges between 100 and around 300 W m^{-2}, with higher values in the north (Figure 3b). It is worthwhile to note that the distribution of surface heat flux is characterized by east-west oriented contours, and this seems to be inconsistent with the distribution of SST (Figure 2a). The effect of ocean dynamics is believed to be responsible for this inconsistency, as discussed below.

3.3. Mixed Layer Depth

The thickness of the surface mixed layer (MLD) is a key factor influencing SST. In some parts of the global ocean, such as the western Pacific warm pool, where MLD is deep, water upwelled from the subsurface is not very much different in temperature from the surface water, and as a result, ocean dynamics has little effect on the surface thermal structure [*Qu et al*., 1997]. However, this does not seem to be the case in the South China Sea, where MLD is shallow and upwelling occurs intermittently throughout the year [*Nitani*, 1972; *Chao et al*., 1996].

MLD, defined using a critical temperature gradient of 0.05°C m^{-1}, is generally deeper than 40 m in the mean, except for a band of shallower values at 15°–19°N, with the East Vietnam eddy on its western side and the West Luzon eddy on its eastern side (Figure 4a). Deeper MLD (>44 m) is observed and drops continuously following the intrusion path of the North Pacific waters along the continental slope south of China [*Qu et al*., 2000]. The largest MLD (>46 m) lies in the central

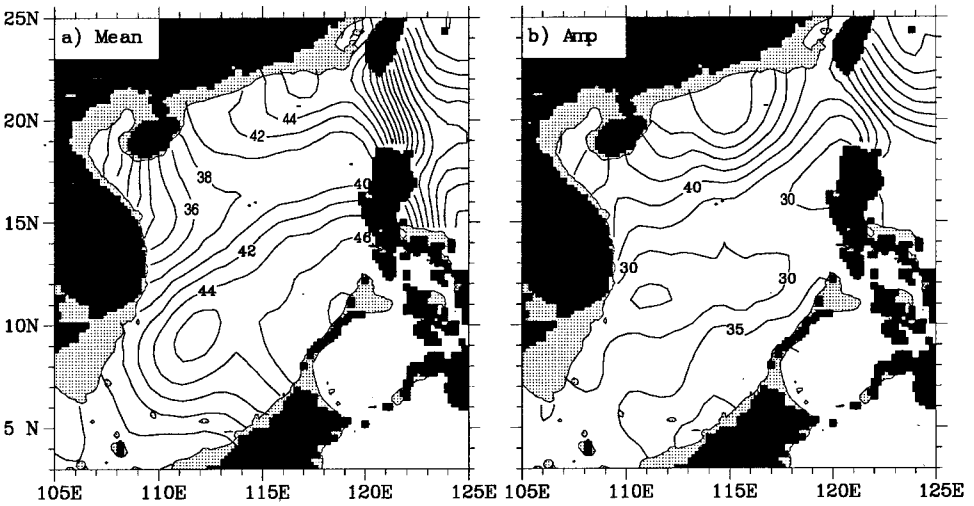

Figure 4. Same as Figure 2 except for mixed layer depth (m) defined using a critical gradient of 0.05°C m^{-1}. Regions with water depth shallower than 50 m are shaded.

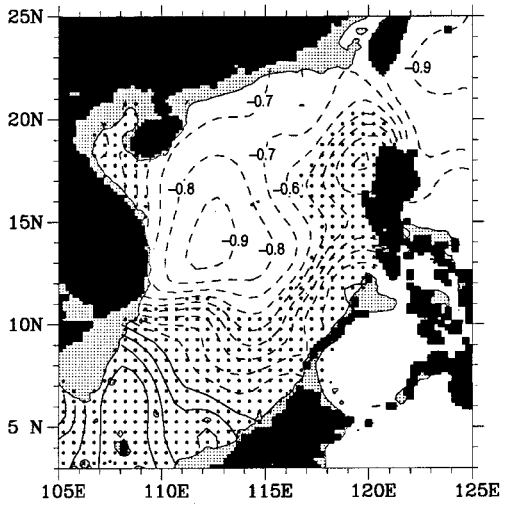

Figure 5. Correlation coefficient between SST and MLD. Asterisks indicate grid points where the criterion of 95% confidence level (t test) is not satisfied. Areas with water depth shallower than 50 m are shaded.

southern South China Sea, coinciding roughly with the spring warm pool [*Chu and Chang*, 1997].

In general, MLD is shallower in spring/summer and deeper in fall/winter. The maximum seasonal variability is observed near the southern coast of China (Figure 4b), where MLD exceeds 80 m in January and shoals quickly to about 20 m in May/June. Elsewhere, the seasonal variability of MLD is smaller but has different phases in different parts of the basin (discussed in section 4).

Given the MLD characteristics described above, the South China Sea can be partitioned into four smaller areas, namely, boxes A, B, C, and D (Figure 1a). Box A is along the continental slope south of China and has deep MLD associated with the intrusion of the North Pacific waters. Box B coincides with the West Luzon eddy. Box C is around the central southern South China Sea and to a certain extent represents the spring warm pool. Box D is identical with the East Vietnam eddy. Below, the seasonal cycles of MLD, SST, and mixed layer heat balance in these areas are examined in detail.

4. Correlation Between SST and MLD

We explore the relationship between SST and MLD to infer the possible influence of ocean dynamics on the surface thermal structure (Figure 5). Over much of the region studied we see a negative correlation between the two variables, with higher SST corresponding with shallower MLD and vice versa, and this negative correlation is particularly evident in the time series averaged over each individual box selected above (Figure 6). From late winter to early spring, as MLD shoals against the diminishing of the northeast monsoon, heat gained from the atmosphere is trapped in a shallower surface mixed layer and eventually warms up the SST. The deepening of MLD forced by the southwest monsoon marks the end of this accumulation of heat, and as a result, SST drops continuously during the rest of the year.

Within the context of mixed layer dynamics, which neglects the influence of horizontal advection and radiative heat flux,

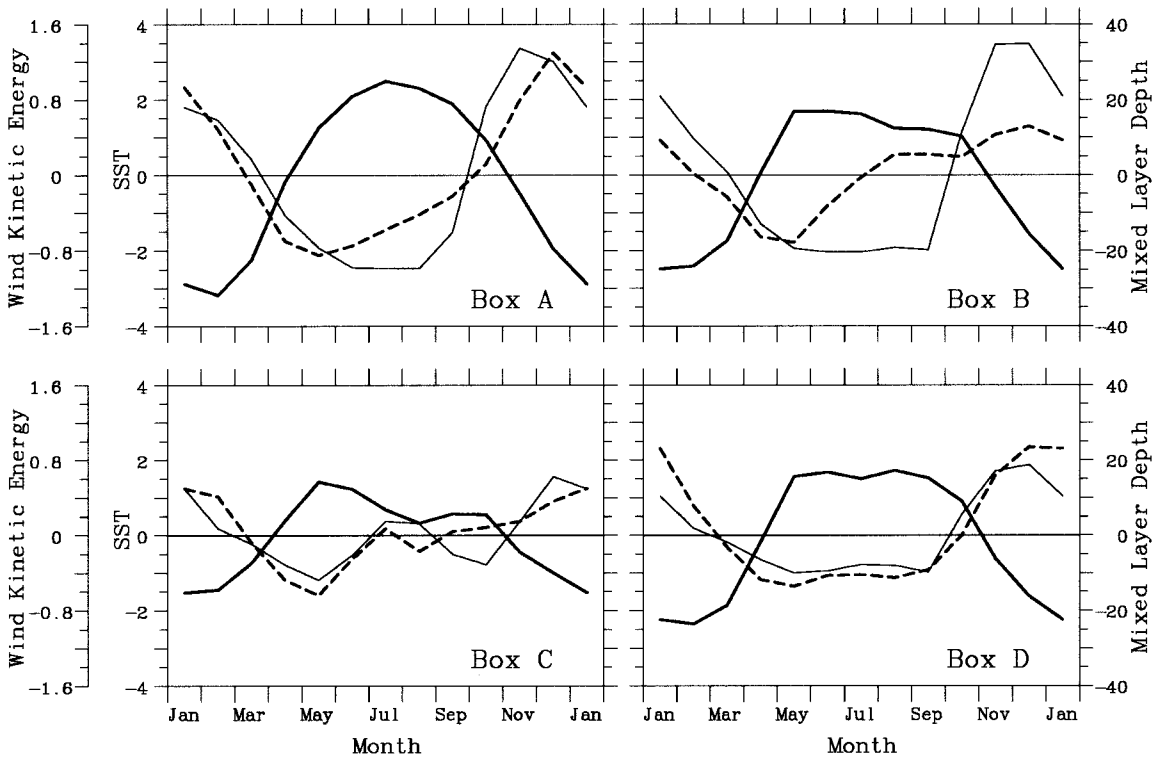

Figure 6. Time series of SST (C°; heavy solid), mixed layer depth (m; heavy dashed), and wind kinetic energy (10^4 Erg m^{-2} s^{-1}; light solid) averaged over boxes A, B, C, and D. Annual mean values have been subtracted before plotting.

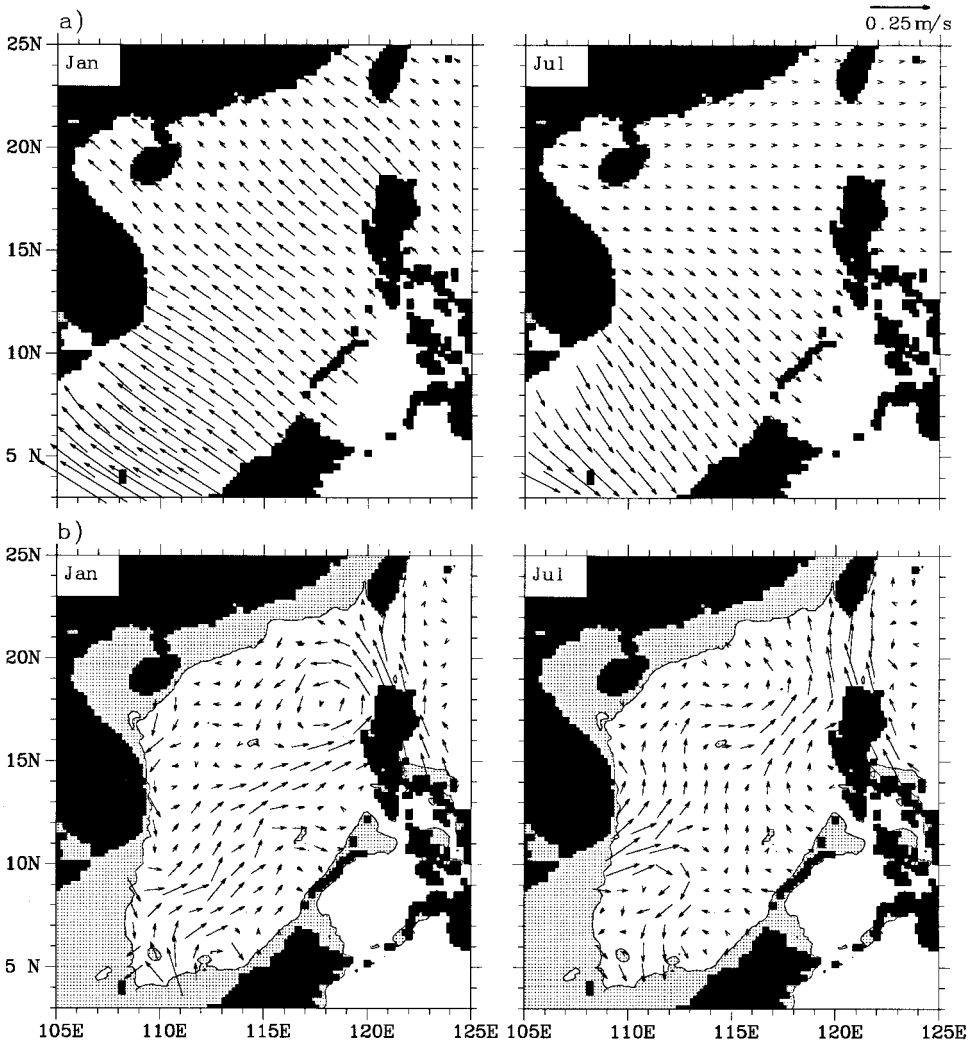

Figure 7. (a) Ekman current calculated from *Hellerman and Rosenstein*'s [1983] wind stress and (b) geostrophic flow derived from *Qu*'s [2000] dynamic height.

the deepening of MLD is a result of entrainment of colder and denser water into the mixed layer from the below and represents a downward flux of buoyancy and an associated increase of potential energy. This increase of potential energy and the mechanical energy required to maintain the necessary turbulence is supplied by the wind, possibly through an energy cascade from surface waves or by sheared currents working against Reynolds stresses [cf. *Davis et al*., 1981]. A simple estimate of the rate of this wind stirring, often called wind kinetic energy, is $\frac{1}{2}\rho u_*^3$, where $u_* = |\tau/\rho|^{1/2}$ is the friction velocity, τ is the surface wind stress, and ρ is the density of sea water [e.g., *Niiler*, 1975]. The temporal correspondence of MLD with wind kinetic energy, computed from *Hellerman and Rosenstein*'s [1983] wind stress in a $1° \times 1°$ horizontal grid, is striking, and the northeast monsoon stands out as a seasonal maximum of both variables for all the four boxes chosen (Figure 6). Wind kinetic energy is relatively weak in summer but explains most of the MLD variability in boxes C and D. The largest discrepancy between the two time series is seen in box B, where MLD deepens rapidly from May to August while wind kinetic energy remains almost unchanged. This discrepancy reflects the strong influence of horizontal advection, Ekman pumping, and radiative heat flux (discussed in section 5).

5. Heat Budget of the Mixed Layer

In order to assess quantitatively the effect of ocean dynamics on the SST we examine below the heat budget of the mixed layer [*Niiler*, 1975; *Davis et al*., 1981; *Qiu*, 2000]:

$$\frac{\partial T_m}{\partial t} = \frac{Q}{\rho C_p h_m} - u_e \cdot \nabla T_m - u_g \cdot \nabla T_m - \frac{w_{\text{ent}}(T_m - T_d)}{h_m}, \qquad (1)$$

where T_m denotes the mixed layer temperature and is a good proxy of SST, h_m is the mixed layer depth, Q is the net surface heat flux, u_e is Ekman velocity, u_g is the geostrophic velocity, w_{ent} is the entrainment rate, T_d is the water temperature below the base of the mixed layer, and $C_p\rho$ is the specific heat capacity per unit volume. In the following we refer to the five terms in (1) as temperature tendency, surface heat flux, Ekman advection, geostrophic advection, and vertical entrainment, respectively [*Qiu*, 2000].

We analyze the mixed layer heat budget (equation (1)) using the upper layer temperature data described in section 2 combined with the climatologies of heat flux [*Oberhuber*, 1988] and wind stress [*Hellerman and Rosenstein*, 1983]. An important assumption made is that both temperature and velocity are independent of depth within the mixed layer [*Niiler*, 1975;

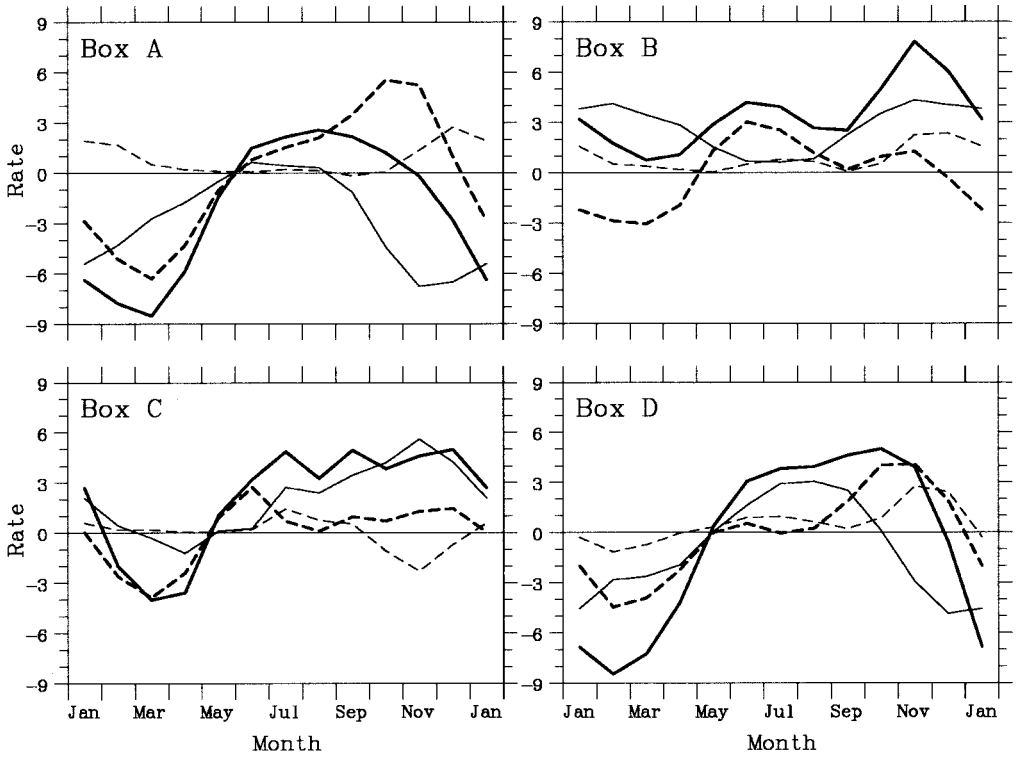

Figure 8. Time series of vertical entrainment/detrainment rate (heavy solid) and its three components: the rate of deepening mixed layer (heavy dashed), Ekman pumping (light solid), and advection (light dashed) due to the slope of the mixed layer base. The unit is 10^{-6} m s^{-1}.

Davis et al., 1981; *Qiu*, 2000]. Homogeneous temperature is how mixed layers are generally defined (section 3.3) and is simply computed as $T_m = 1/h_m \int_{-h_m}^{0} T(z)\, dz$, where $T(z)$ denotes monthly mean temperature with a 10 m vertical resolution (section 2). The temperature jump across the base of the mixed layer, $T_m - T_d$, is determined by choosing T_d at a depth of 5 m below $-h_m$, where turbulent and radiative heat fluxes are assumed to be negligible.

The assumption of unsheared flow within the mixed layer is more controversial [*Davis et al*., 1981] given that the ocean is populated with internal waves and mesoscale eddies of various sizes and durations. We note, however, that our analysis focuses only on that component of flow generated by large-scale forcing; those associated with internal waves and mesoscale eddies are excluded from this study.

5.1. Horizontal Circulation

Before proceeding further to the heat budget analysis, we first examine the mixed layer circulation of the South China Sea, which can be further decomposed into the Ekman current and geostrophic flow.

5.1.1. Ekman current. We define the Ekman velocity by $u_e = \tau \times k/(\rho f h_m)$, where τ is the surface wind stress vector and f is the Coreolis parameter. The annual cycle of the surface wind [*Hellerman and Rosenstein*, 1983] in the South China Sea is dominated by the northeast monsoon in winter and the southwest monsoon in summer. The northeast monsoon begins to appear in the northern South China Sea in September and reaches its maximum strength in December and January, leading to a northwestward Ekman transport over the entire basin (Figure 7a). The southwest monsoon first appears in the central South China Sea in May/June and expands northward in the following months. Its resulting Ekman current is somewhat weaker and is confined in a smaller area compared with the case for the northeast monsoon, basically to the south of 18°N (Figure 7b).

5.1.2. Geostrophic flow. The geostrophic flow field used here has been discussed and derived by *Qu* [2000] from upper layer temperature data combined with climatological temperature-salinity relationships [*Meyers et al*., 1995]. Here we simply average it within the mixed layer and provide a brief description in Figure 7b. In winter, when prevailing wind is from the northeast, geostrophic flow contains a large cyclonic gyre with a broad northeastward flow in the central part of the basin and a narrow southwestward flow along the continental slope south of China. In summer the northeastward flow becomes widely spread in response to the southwest monsoon, with the maximum velocity of the order 0.2 m s^{-1}.

A major concern one might raise with *Qu*'s [2000] estimate of geostrophic flow is his adoption of a reference level at 400 dbar. Synoptic measurements collected during the South China Sea Monsoon Experiment (SCSMEX) [*Lau*, 1998] have shown a significant deep component of velocity, sometimes larger than 0.1 m s^{-1}, around 400 dbar. In this light our estimate of geostrophic flow may not be especially accurate without further information on deeper currents and better reference levels. We note, however, that synoptic measurements include motions from other sources, such as tides, internal waves, and mesoscale eddies, which are beyond the focus of the present study. In addition, geostrophic flow tends to follow isothermal surfaces, given that the effect of salinity on water density is less important than temperature in the upper layers of the tropical western Pacific and its surrounding seas [*Qu et al*., 1999], and

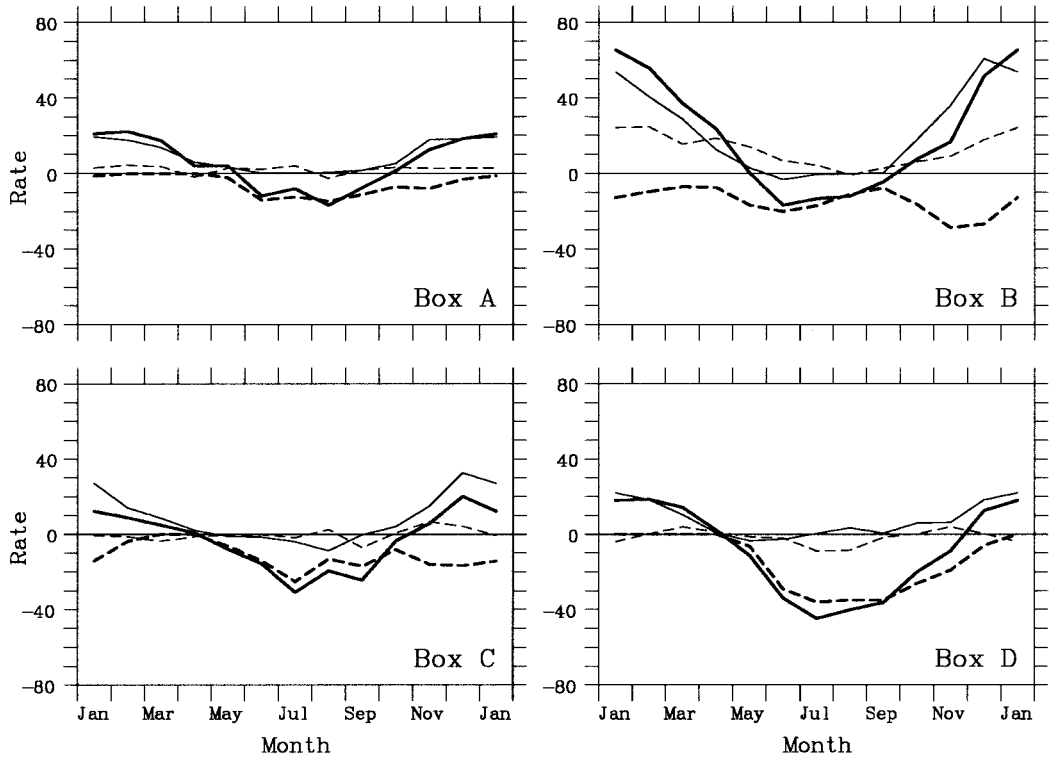

Figure 9. Time series of Ekman (light solid) and geostrophic (light dashed) advection and vertical entrainment (heavy dashed) and sum of the three terms (heavy solid) in the mixed layer. Unit is 10^{-8} °C s^{-1}.

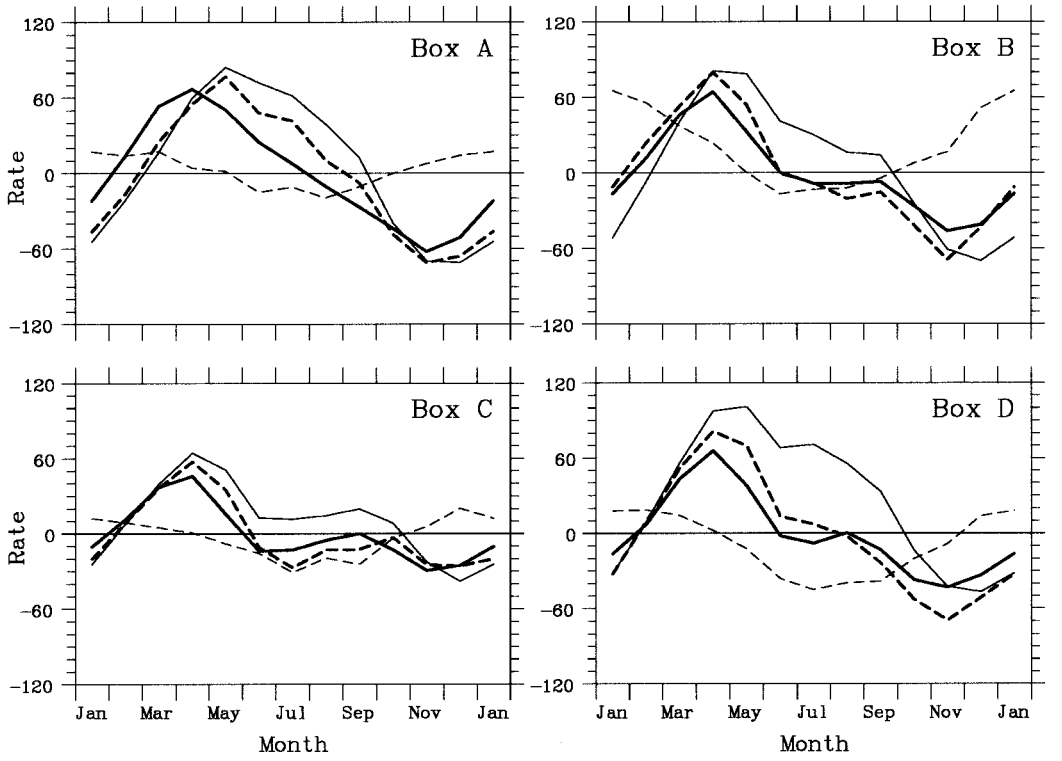

Figure 10. Time series of temperature tendency (heavy solid), surface heat flux (light solid), sum of Ekman and geostrophic advection and vertical entrainment (light dashed), and sum of surface heat flux, Ekman and geostrophic advection, and vertical entrainment (heavy dashed). Here annual mean values of 9.0, 24.8, 7.8, and 18.5 have been subtracted in boxes A, B, C, and D, respectively, before plotting the sum of surface heat flux, Ekman and geostrophic advection, and vertical entrainment. Unit is 10^{-8} °C s^{-1}.

Table 1. Linear Correlation Coefficient Between $\partial T_m/\partial t$ and Q and Between $\partial T_m/\partial t$ and $Q + hD + vE$[a]

	Box A	Box B	Box C	Box D
$\partial T_m/\partial t$ versus Q	0.79	0.85	0.85	0.80
$\partial T_m/\partial t$ versus $Q + hD + vE$	0.89	0.99	0.95	0.98

[a]Here $\partial T_m/\partial t$ denotes the temperature tendency, Q denotes the surface heat flux, hD denotes the heat advection due to horizontal circulation, and vE denotes the vertical entrainment.

as a result, temperature gradient in the direction of geostrophic flow is expected to be small. On the basis of the upper layer temperature data described in section 2 we obtain that the temperature gradient in the direction of geostrophic flow (Figure 7b) is smaller, typically by a factor 2, than that of Ekman current (Figure 7a), and it increases to as large as 4 in the central South China Sea (box C). The small temperature gradient in the direction of geostrophic flow downplays the effect of geostrophic advection, as will be seen in section 5.3. Under this circumstance it is unlikely that the correction to geostrophic advection due to the uncertainty of reference velocity can alter the basic balance of (1).

5.2. Entrainment/Detrainment Rate

The entrainment rate w_{ent}, defined as the volume flux of the thermocline water entering the mixed layer per unit horizontal area at the base of the mixed layer, is determined according to the rate of the mixed layer deepening, $\partial h_m/\partial t$, the vertical velocity of water parcel at the base of the mixed layer, w_{mb}, and the horizontal advection of water parcels below the mixed layer, $u \cdot \nabla h_m$ [e.g., *Cushman-Roisin*, 1987; *Williams*, 1989], i.e.,

$$\begin{aligned} w_{\text{ent}} &= \frac{\partial h_m}{\partial t} + w_{mb} + u \cdot \nabla h_m, & \frac{\partial h_m}{\partial t} + w_{mb} + u \cdot \nabla h_m > 0 \\ w_{\text{ent}} &= 0, & \frac{\partial h_m}{\partial t} + w_{mb} + u \cdot \nabla h_m \le 0. \end{aligned} \tag{2}$$

In a similar way we define the detrainment rate w_{det} as the volume flux of the mixed layer water entering the thermocline per unit horizontal area at the base of the mixed layer, i.e.,

$$\begin{aligned} w_{\text{det}} &= -\left(\frac{\partial h_m}{\partial t} + w_{mb} + u \cdot \nabla h_m\right), & \frac{\partial h_m}{\partial t} + w_{mb} + u \cdot \nabla h_m < 0 \\ w_{\text{det}} &= 0, & \frac{\partial h_m}{\partial t} + w_{mb} + u \cdot \nabla h_m \ge 0. \end{aligned} \tag{3}$$

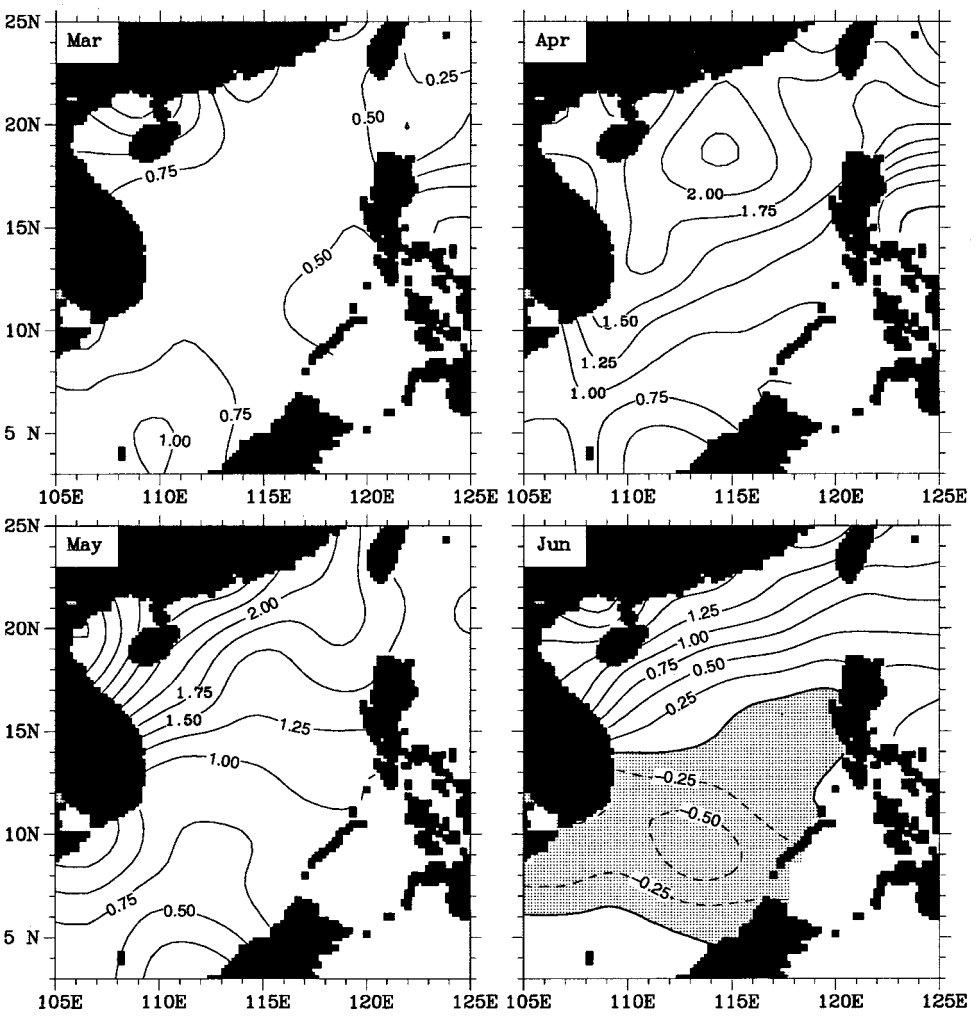

Figure 11. The tendency of SST (°C) as the change from its previous month. Regions with negative values are shaded.

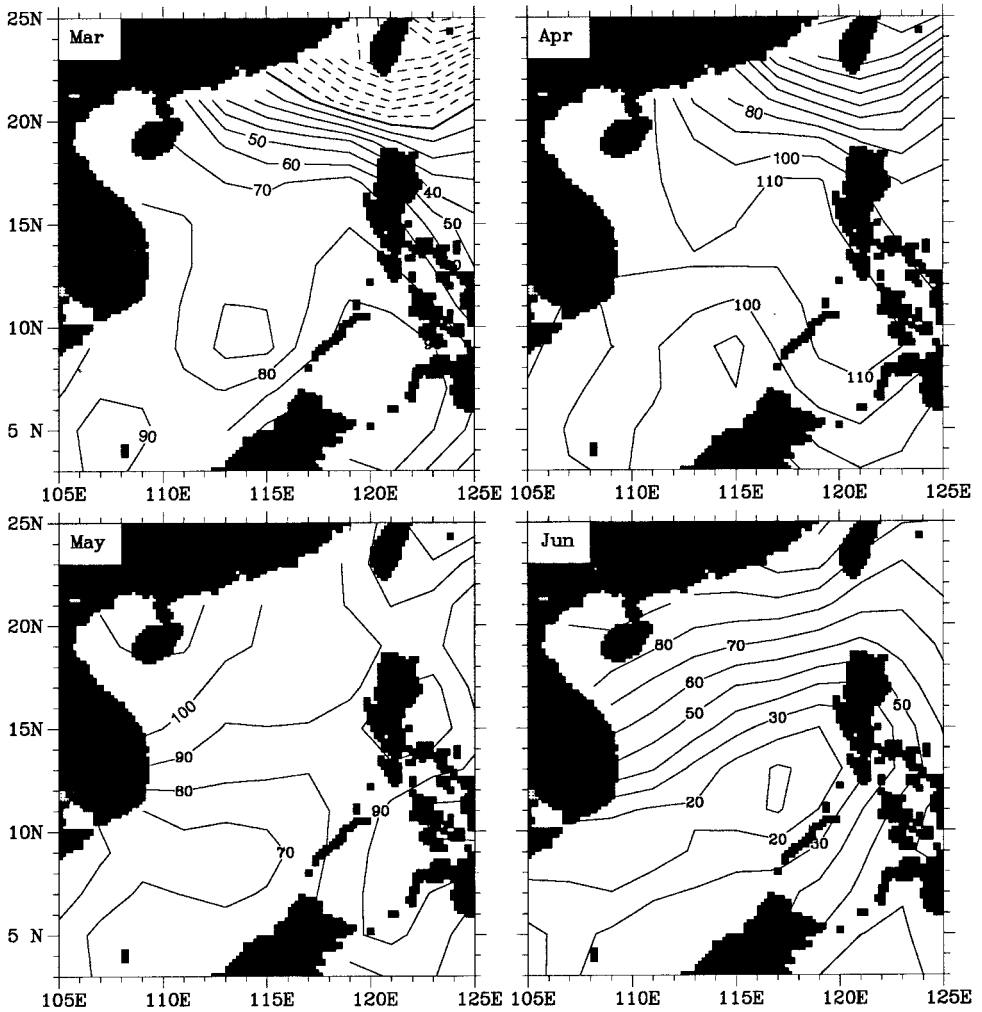

Figure 12. Surface heat flux (W m^{-2}) in *Oberhuber*'s [1988] climatology.

Here, $w_{mb} = w_{\text{emb}} + w_{\text{gmb}}$, $u \cdot \nabla h_m = u_e \cdot \nabla h_m + u_g \cdot \nabla h_m$, and the subscripts e and g denote Ekman and geostrophic component, respectively.

It is commonly believed that in the region where MLD is shallow, vertical velocity at the base of the mixed layer is dominated by Ekman pumping. Our estimate further suggests that the entrainment rate in the South China Sea is primarily a result of counterbalance between $\partial h_m/\partial t$ and w_{emb}; contribution from geostrophic flow (i.e., $w_{\text{gmb}} + u_g \cdot \nabla h_m$) is negligibly small. The seasonal variations of entrainment rate and its two components induced by Ekman current (i.e., w_{emb} and $u_e \cdot \nabla h_m$) are described in Figure 8.

Ekman pumping in box A is mostly downward, reaching its maximum strength ($<-6 \times 10^{-6}$ m s^{-1}) in winter and minimum strength (close to zero) in summer. Combined with the rate of MLD deepening, this leads to an entrainment from June to November and a detrainment during the rest of the year. Advection of water parcels due to the slope of the mixed layer base also contributes in winter, but its magnitude is small relative to the other two components shown above.

Box B coincides with the West Luzon eddy, where Ekman pumping is upward all year round [*Qu*, 2000]. Its magnitude exceeds 4×10^{-6} m s^{-1} in winter and drops to near zero in summer. Although the rate of MLD shoaling cancels out part of this Ekman pumping from later winter to early spring, colder and denser waters are entrained from below into the mixed layer during all seasons of the year.

Box C is around the zero wind stress curl line, and as a result, Ekman pumping is significant only from late fall to early winter. Rapid shoaling of MLD occurs from January to May against the diminishing northeast monsoon, which, together with the Ekman pumping, results in a detrainment from February to May and an entrainment during the rest of the year.

The condition of vertical entrainment in box D is somewhat similar to that in box A, and this probably reflects the northeast-southwest orientation of wind stress curl [*Qu*, 2000]. The only significant difference between the two areas is that Ekman pumping tends to produce a stronger entrainment in box D, lasting for a period from May to December with maximum magnitude exceeding 5×10^{-6} m s^{-1}.

5.3. Heat Advection and Entrainment

To estimate the advective and vertical entrainment terms of (1), we interpolate horizontal circulation and entrainment rate onto a monthly 0.5° × 0.5° grid. Individual terms are then calculated and averaged for each box. During the northeast monsoon, as water entering each box is higher in temperature usually by a few degrees than water leaving it, Ekman advection acts as the primary heating process for the region (Figure 9). The horizontal temperature gradient is much reduced in

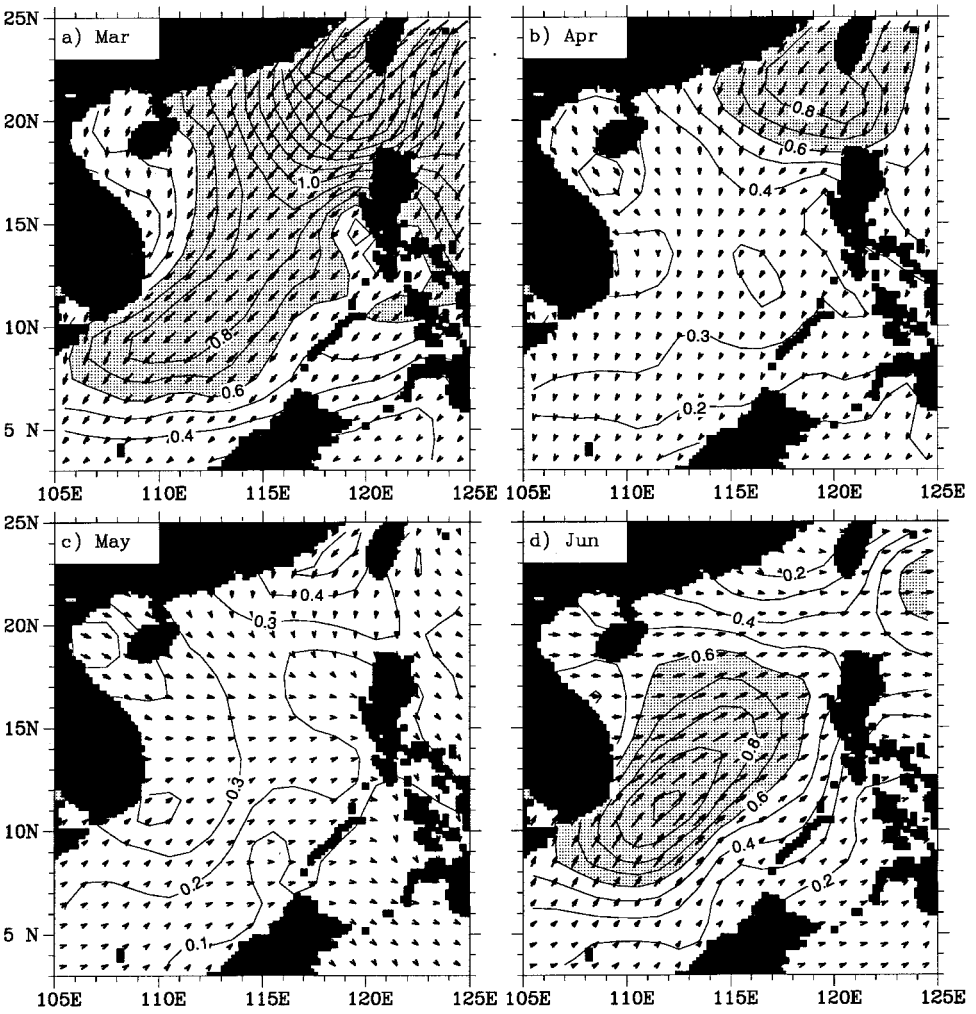

Figure 13. Wind stress (10^{-1} N m^{-2}) in *Hellerman and Rosenstein*'s [1983] climatology. Regions greater than 0.06 N m^{-2} are shaded.

summer, and as a result, vertical entrainment becomes more effective at cooling than horizontal advection, even though Ekman current is from the northwest.

On closer inspection of individual boxes we see that vertical entrainment does not work effectively from late winter to early spring, except for box B, where it occurs continuously throughout the year as a result of Ekman pumping. Advection by geostrophic flow is rather weak in comparison with that by Ekman current, as a result of small temperature gradient (section 5.1). The largest geostrophic advection ($\sim 20 \times 10^{-8}$ °C s^{-1}) occurs in box B; still, it accounts for only about one third of the total horizontal advection. The cancellation between Ekman advection and vertical entrainment leads to a heating in winter and a cooling in summer in all four boxes, with its magnitude $>60 \times 10^{-8}$ °C s^{-1} in box B and $<-40 \times 10^{-8}$ °C s^{-1} in box D.

5.4. Net Heat Balance

Adding all terms of (1), we obtain a net heat balance of the mixed layer (Figure 10). In all four boxes, surface heat flux is by far the most important process that determines the mixed layer temperature, but the effect of heat advection and vertical entrainment is not negligible.

In box A the temperature tendency reaches its seasonal maximum ($\sim 70 \times 10^{-8}$ °C s^{-1}) in April and its minimum ($\sim -60 \times 10^{-8}$ °C s^{-1}) in November, while surface heat flux lags by 1–2 months, heating the ocean from March to September and cooling it during the rest of the year. This difference in phase is also evident in boxes B and D but somewhat smaller in box C. Adding the contribution from heat advection and vertical entrainment better explains the temperature tendency, and as a result, the difference in phase between the two terms just mentioned above is significantly narrowed.

Further inspection indicates that temperature decreases ($\partial T_m/\partial t < 0$) during the southwest monsoon, even if the ocean is being heated. In the central South China Sea (box C), in particular, the decrease of temperature first appears in May, earlier by about 5 months than surface heat flux starts to cool the ocean. The surface heat flux during that period of time is usually larger than 20×10^{-8} °C s^{-1} and can be as large as 70×10^{-8} °C s^{-1} (box D); much of this surface heating is counterbalanced by vertical entrainment.

As a summary of this section, we show the correlation coefficient between the temperature tendency and surface heat flux (Table 1). In all the four boxes chosen this correlation coefficient is of the order 0.80 but increases significantly when the contribution from heat advection and vertical entrainment is

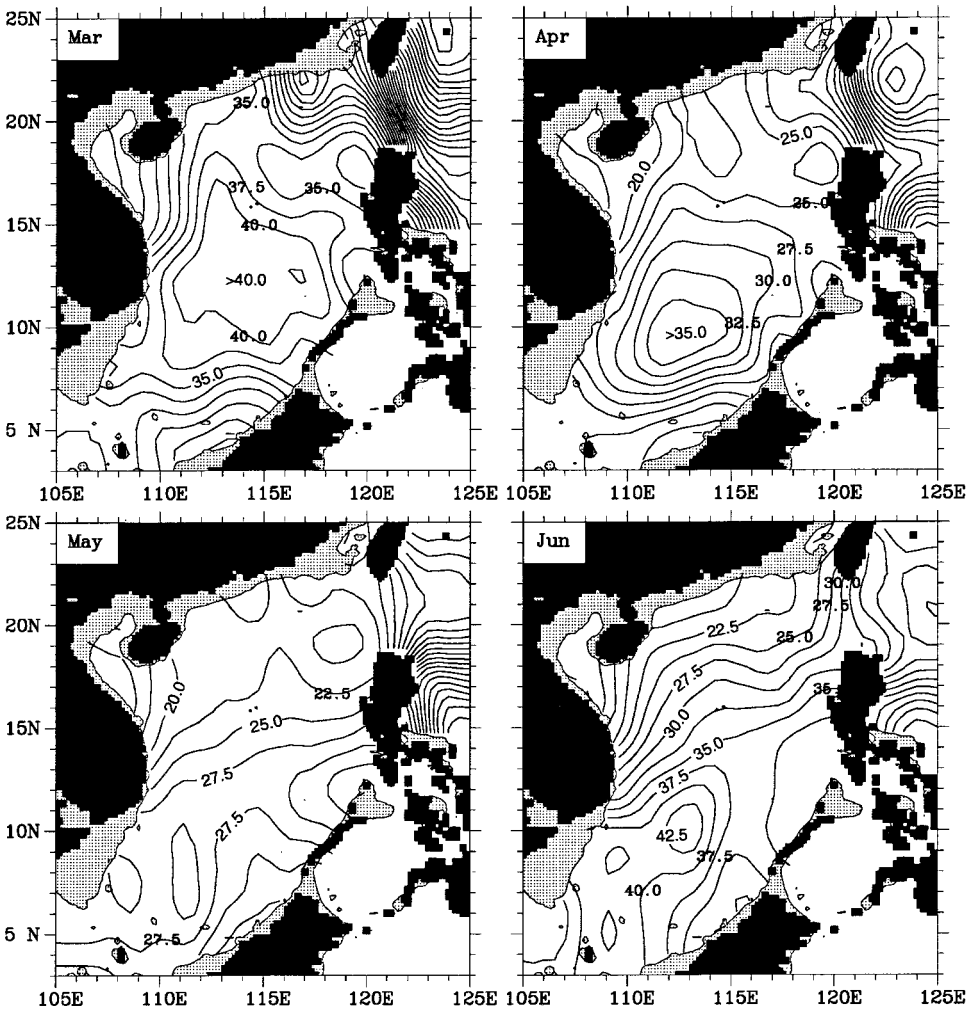

Figure 14. Mixed layer depth (m) defined using a critical temperature gradient of 0.05°C m^{-1}. Regions with water depth shallower than 50 m are shaded.

included, reaching 0.89 in box A, 0.99 in box B, 0.95 in box C, and 0.98 in box D. This increased correlation coefficient clearly demonstrates the importance of ocean dynamics in determining the mean seasonal cycle of the South China Sea surface temperature.

6. Dynamics Related to the Onset of Southwest Monsoon

In this section we examine how ocean dynamics works against the incoming surface heat flux during the southwest monsoon. Instead of showing the anomaly field for each individual month, Figure 11 illustrates the tendency of SST or the change of SST from its previous month. SST increases slightly in March, and as more heat enters the ocean from the atmosphere (Figure 12), it warms up dramatically in April/May, with the maximum monthly change exceeding 2.0°C in the north. The seasonal maximum of SST appears in May in the central basin, roughly coinciding with the spring warm pool [*Chu and Chang*, 1997] and somewhat later on either side of it. The onset of the southwest monsoon in June (Figure 13) marks the end of the spring warm pool (Figure 11), and SST drops continuously after that to its seasonal minimum in January.

In addition to surface heat flux, ocean dynamics is also important in determining the seasonal variation of SST (section 6). From late winter to early spring, as the northeast monsoon diminishes (Figure 13), wind stress cannot provide enough turbulent kinetic energy to overcome the buoyancy force in order to maintain the deep mixed layer created in winter, and as a result, MLD shoals rapidly over the basin (Figure 14). The spatial distribution of MLD in March and April suggests the existence of a basin-wide anticyclonic circulation. Recent studies [e.g., *Wu et al*., 1998; *Shaw et al*., 1999] have reported a similar pattern of sea level and horizontal velocity using empirical orthogonal function (EOF) analysis. Though this mode (the second mode of their EOF analysis) explains only a small part of the total variance, about 8% for sea level and 10% for horizontal velocity, it has extreme positive values around April and dominates both sea level and horizontal velocity fields at that time. *Wu et al*. [1998] further noted that this anticyclonic circulation is largely caused by wind stress curl.

MLD reaches its seasonal minimum (<30 m) in May, when the spring warm pool (>29.5°C) is forced in the central South China Sea. The occurrence of the spring warm pool could be a result of weak wind stress, which drops to 0.03 N m^2 or less in May in much of the basin (Figure 13). In the mean time a large

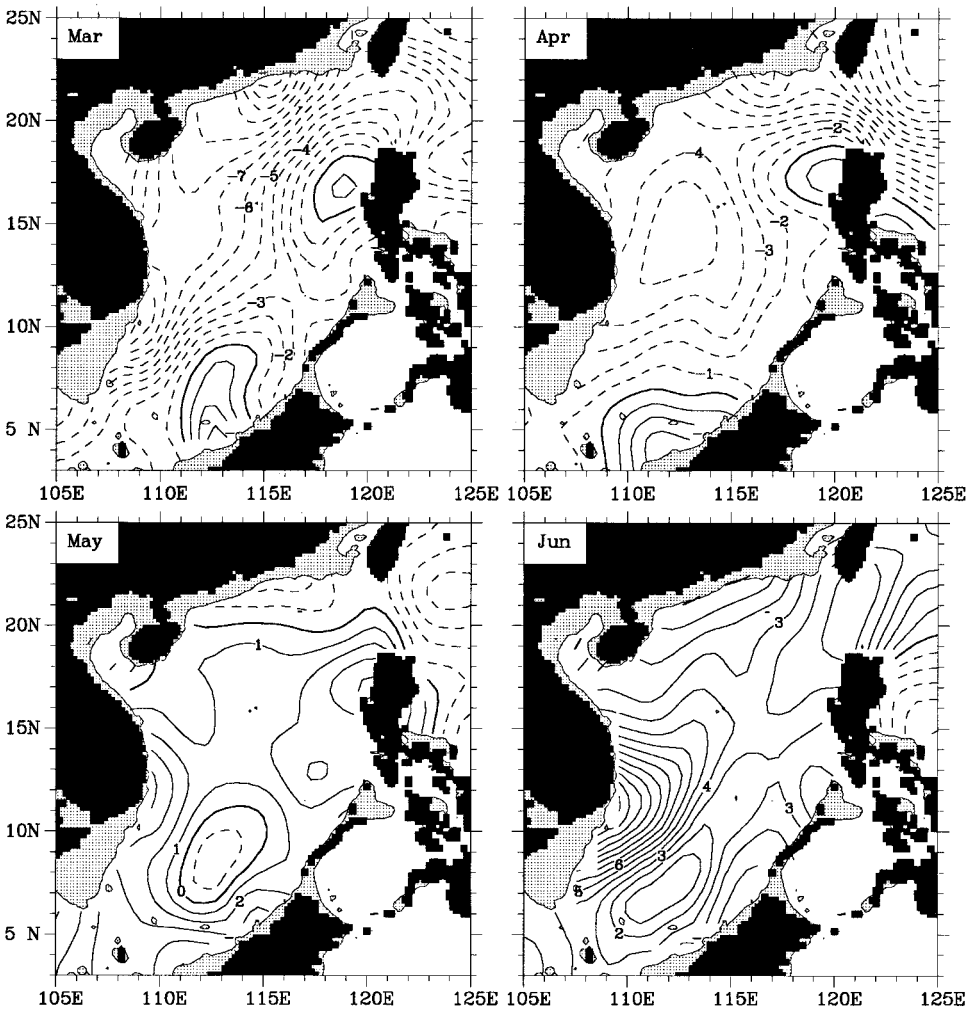

Figure 15. Entrainment/detrainment rate (10^{-6} m s^{-1}) at the base of the mixed layer. Positive (negative) values indicate entrainment (detrainment). Regions with water depth shallower than 50 m are shaded.

amount ($\sim$100 W m^{-2}) of heat enters the ocean from the atmosphere (Figure 12), making an additional contribution to the heating of the surface mixed layer. The developing seasonal pycnocline as a result of continuous detrainment from March to May prevents the incoming surface heat flux from being transported downward (Figure 15).

Wind stress starts to intensify in June, except for a small region west of Taiwan. As the southwest monsoon appears in the central basin (Figure 13), MLD deepens immediately, exceeding 40 m in the vicinity of the high wind stress core ($>$0.1 N m^{-2}) southeast of Vietnam (Figure 14), and as a consequence, colder and denser thermocline waters are entrained into the mixed layer (Figure 15). In addition, enhanced evaporation associated with the development of the southwest monsoon causes significant latent heat loss to the atmosphere [*Chu and Chang*, 1997], as indicated by a low surface heat flux belt ($<$20 W m^{-2}) in the spring warm pool region (Figure 12). The combined effect of entrainment at the base of the mixed layer and enhanced evaporation sets down the SST in June in the central basin (Figure 11) and somewhat later elsewhere.

Ose et al. [1997] suggested that the SST anomaly in summer does not control the atmosphere but is controlled by the atmospheric circulation related to the summer Asian monsoon. Indeed, we find that the onset of the southwest monsoon is chiefly responsible for the decrease of SST in late spring and early summer. However, we emphasize that the effect of SST anomaly on the atmosphere is not negligible. The occurrence of the spring warm pool, for example, contributes to the lowering of surface pressure and in turn to the development of the summer monsoon [*Chu and Chang*, 1997]. The details have to be investigated further by research.

7. Summary

Although it is conceivable that the seasonal reversing monsoon and its derived circulation might play a role in influencing the South China Sea surface temperature, their exact role is not known. A combined use of historical temperature data with wind stress and surface heat flux climatologies provides us with a quantitative description of the mean seasonal cycle of surface heat budget.

We find that SST and MLD are negatively correlated over a large part of the South China Sea. Considering the characteristics of the MLD distribution, we further partition the basin into four smaller areas: one along the intrusion path of the North Pacific waters and the others representing the West Luzon eddy, central spring warm pool, and east Vietnam eddy, respectively. Heat budget assessment in these smaller areas

suggests that surface heat flux is fundamental to the seasonal variation of SST, but the effect of ocean dynamics is not negligible.

Ekman advection is the primary heating process in winter but becomes negligibly small as horizontal temperature gradient decreases in summer. In comparison, geostrophic advection is less important because the temperature gradient in the direction of geostrophic flow is smaller typically by a factor 2–4 than that in the direction of Ekman current. At least on the seasonal timescale, geostrophic advection does not appear to play a significant role in influencing the South China Sea surface temperature.

Vertical entrainment is effective at cooling in summer. During the southwest monsoon, enhanced turbulent kinetic energy provided by wind stress leads to a quick MLD deepening. Combined with direct Ekman pumping, this represents a transfer of water into the mixed layer from below and eventually a cooling of SST in most parts of the South China Sea.

The present data confirm the existence of the spring warm pool, which appears in May but decays soon after the southwest monsoon develops in the central South China Sea. The decay of the spring warm pool cannot be explained by the seasonal fluctuation of surface heat flux, which does not reverse sign until some 5 months after the spring warm pool starts to decay. Adding vertical entrainment forced by the southwest monsoon better explains this temperature tendency.

Finally, we note that because of data limitations, the present study neglects contributions from small-scale ($<$30 days) processes, such as vertical buoyancy flux $-g\overline{w'\rho'}$ and heat flux $-g\overline{w'T'}$, where the quantities with primes represent perturbations from their respective monthly mean values. By neglecting these contributions we might have underestimated the effect of vertical entrainment, which as a result, has led to positive residuals in the mean annual heat budget (Figure 10). For this concern our estimate of the mean seasonal cycle of the surface heat budget may be modified somewhat as more observational data become available. However, in a qualitative sense we believe that most of our conclusions will remain valid.

Acknowledgments. This research was supported by Frontier Research System for Global Change through its sponsorship of the International Pacific Research Center (IPRC). The author is grateful to T. Yamagata, G. Meyers, J. P. McCreary, and H. Mitsudera for valuable discussions and to J. Toole for constructive suggestions throughout the study. Thanks are also extended to S. K. Behera and Y. Masumoto for valuable discussions on the present topic and to D. Henderson and two anonymous reviewers for useful comments on the earlier manuscript. School of Ocean and Earth Science and Technology (SOEST) contribution 5296. IPRC contribution IPRC-66.

References

Chao, S.-Y., P.-T. Shaw, and S. Y. Wu, Deep sea ventilation in the South China Sea, *Deep Sea Res*., *Part I*, *43*, 445–466, 1996.

Chu, P. C., and C. P. Chang, South China Sea warm pool in boreal spring, *Adv. Atmos. Sci*., *14*, 195–206, 1997.

Chu, P. C., S. Lu, and Y. Chen, Temporal and spatial variabilities of the South China Sea surface temperature anomaly, *J. Geophys. Res*., *102*, 20,937–20,955, 1997.

Chu, P. C., Y. Chen, and S. Lu, Wind driven South China Sea deep basin warm-core/cool-core eddies, *J. Oceanogr*., *54*, 347–360, 1998.

Cushman-Roisin, B., Subduction, paper presented at 'Aha Huliko 'a Hawaiian Winter Workshop, School of Ocean Sci. and Technol., Univ. of Hawaii at Manoa, Honolulu, 1987.

Davis, R. E., R. deSzoeke, and P. P. Niiler, Variability in the upper ocean during MILE, part II, Modeling the mixed layer response, *Deep Sea Res*., *Part A*, *28*, 1453–1475, 1981.

He, Y., C. Guan, and Z. Gan, Interannual and interdecadal variations in heat content of the upper ocean of the South China Sea, *Adv. Atmos. Sci*., *14*, 271–276, 1997.

Hellerman, S., and M. Rosenstein, Normal monthly wind stress over the world ocean with error estimates, *J. Phys. Oceanogr*., *13*, 1093–1104, 1983.

Lau, K.-M., The South China Sea Monsoon Experiments (SCSMEX), *Eos Trans. AGU*, *78*, 599, 603, 1998.

Levitus, S., Climatological atlas of the world oceans, *NOAA Prof. Pap*., *13*, U.S. Gov. Print. Off., Washington, D. C., 1982.

Meyers, G., R. J. Bailey, and A. P. Worby, Geostrophic transport of Indonesian Throughflow, *Deep Sea Res*., *Part I*, *42*, 1163–1174, 1995.

Niiler, P. P., Deepening of the wind-mixed layer, *J. Mar. Res*., *33*, 405–422, 1975.

Nitani, H., Beginning of the Kuroshio, in *Kuroshio: Physical Aspects of the Japan Current*, edited by H. Stommel and K. Yoshida, pp. 129–163, Univ. of Wash. Press, Seattle, 1972.

Oberhuber, J. M., An atlas based on the "COADS" data set: The budgets of heat, buoyancy and turbulent kinetic energy at the surface of the global ocean, *Rep. 15*, Max Planck Inst. für Meteorol., Hamburg, Germany, 1988.

Ose, T., Y. Song, and A. Kitoh, Sea surface temperature in the South China Sea: An index for the Asian monsoon and ENSO system, *J. Meteorol. Soc. Jpn*., *75*, 1091–1107, 1997.

Qiu, B., International variability of the Kuroshio Extension system and its impact on the wintertime SST field, *J. Phys. Oceanogr*., *30*, 1486–1502, 2000.

Qu, T., Upper layer circulation in the South China Sea, *J. Phys. Oceanogr*., *30*, 1450–1460, 2000.

Qu, T., G. Meyers, S. J. Godfrey, and D. Hu, Upper ocean dynamics and its role in maintaining the annual mean western Pacific warm pool in a global GCM, *Int. J. Climatol*., *17*, 711–724, 1997.

Qu, T., H. Mitsudera, and T. Yamagata, A climatology of the circulation and water mass distribution near the Philippine coast, *J. Phys. Oceanogr*., *29*, 1488–1505, 1999.

Qu, T., H. Mitsudera, and T. Yamagata, The intrusion of the North Pacific waters into the South China Sea, *J. Geophys. Res*., *105*, 6415–6424, 2000.

Shaw, P.-T., S.-Y. Chao, and L.-L. Fu, Sea surface height variations in the South China Sea from satellite altimetry, *Oceanol. Acta*, *22*, 1–17, 1999.

Shen, S., and K.-M. Lau, Biennial oscillation associated with the East Asian Summer Monsoon and tropical sea surface temperature, *J. Meteorol. Soc. Jpn*., *73*, 105–124, 1995.

Tomita, T., and T. Yasunari, Role of the northeast winter monsoon on the biennial oscillation of the ENSO/monsoon system, *J. Meteorol. Soc. Jpn*., *74*, 399–413, 1996.

Williams, R. G., The influence of air-sea interaction on the ventilated thermocline, *J. Phys. Oceanogr*., *19*, 1255–1267, 1989.

Wu, C.-R., P.-T. Shaw, and S.-Y. Chao, Seasonal and interannual variation of the velocity field of the South China Sea, *J. Oceanogr*., *54*, 361–372, 1998.

T. Qu, International Pacific Research Center, SOEST, University of Hawaii, 2525 Correa Road, Honolulu, HI 96822. (tangdong@soest.hawaii.edu)

(Received June 6, 2000; revised November 10, 2000; accepted December 5, 2000.)